Study of ArO^- and ArO via Slow Photoelectron Velocity-Map Imaging Spectroscopy and *Ab Initio* Calculations[†]

Etienne Garand,[‡] Alexei A. Buchachenko,[*,§] Tara I. Yacovitch,[‡] Małgorzata M. Szcześniak,[||] Grzegorz Chałasiński,[||,⊥] and Daniel M. Neumark[*,‡,#]

Department of Chemistry, University of California, Berkeley, California 94720, Laboratory of Molecular Structure and Quantum Mechanics, Department of Chemistry, Moscow State University, Moscow 119991, Russia, Department of Chemistry, Oakland University, Rochester, Michigan 48309, Faculty of Chemistry, University of Warsaw, Pasteura 1, 02-093 Warszawa, Poland, and Chemical Sciences Division, Lawrence Berkeley National Laboratory, Berkeley, California 94720

Received: December 23, 2008; Revised Manuscript Received: January 23, 2009

The high-resolution photoelectron spectrum of ArO^- was obtained using slow electron velocity-map imaging (SEVI). The SEVI spectrum reveals well-resolved vibrational transitions between multiple electronic states of ArO^- and ArO, both of which are open-shell species. These transitions occur within the broad envelope of previous lower resolution photoelectron spectra. Detailed assignments are made by comparison with theoretical simulations based on high level *ab initio* calculations and an atoms-in-molecule model that accounts for spin−orbit coupling in the anion and neutral. The adiabatic electron affinity of ArO is found to be 12481 ± 2 cm^{-1}. Several ArO^- and ArO vibrational frequencies and excited-state term energies are accurately determined from the analysis of the experimental spectra and are found to be in excellent agreement with the calculated values.

I. Introduction

Photoelectron (PE) spectroscopy of molecular anions is a versatile method for determining electron affinities, excited-state term energies, and vibrational frequencies of the corresponding neutral species.[1] A higher resolution variant of this technique, anion zero energy kinetic energy (ZEKE) spectroscopy,[2] has been applied to the study of open-shell van der Waals complexes via photodetachment of the appropriate anion.[3,4] Thus, for example, photodetachment of a rare gas halide such as $ArCl^-$ accesses the ground and low-lying electronic states of the ArCl van der Waals complex.[5] The spectral resolution of ZEKE, 1−3 cm^{-1}, reveals the individual vibrational levels supported by these electronic states that are otherwise difficult to access, and is thus highly complementary to scattering experiments on the same systems.[6] Accurate experimental spectroscopic constants on both the anion and neutral complexes can then be extracted from the spectra which provide a stringent test for the *ab initio* calculated interaction potentials of these species.

Here, we study the related species, ArO^- and ArO, using the recently developed slow electron velocity-map imaging (SEVI) technique, which offers comparable resolution to ZEKE but is considerably easier to implement.[7] The species investigated here are more complex than the rare gas halides, since both the anion and neutral are open-shell species with $^2\Sigma^+$ and $^3\Pi$ ground states, respectively. In addition, there are more low-lying neutral electronic states for ArO than for the rare gas−halogen complexes. Hence, the extraction of accurate potential energy curves for the anion and neutral poses a challenge for both experiment and theory.

Early studies on the rare gas oxides were motivated by their possible application in excimer lasers.[8−10] The first experimental data on the interaction potential between Ar and oxygen atom was obtained from the total scattering cross section experiments of Aquilanti and co-workers.[11−15] Ma et al.[16] measured the relative differential cross section for inelastic intramultiplet transitions for oxygen colliding with Ar. Bowen and co-workers[17,18] have studied ArO^- via PE spectroscopy. The resolution of their apparatus (∼200 cm^{-1}) did not allow the observation of individual vibronic transitions. However, a bimodal structure with temperature dependent relative intensity was observed and attributed to transitions originating from the ground state and the two low-lying excited states of the anion.

On the theoretical side, Buchachenko et al.[19] have implemented an atoms-in-molecule approach to construct potential energy curves for the anion and neutral electronic states, including spin−orbit coupling, and have simulated the ArO^- PE spectrum using these curves. Unrestricted fourth-order Moller−Plesset perturbation theory (UMP4) *ab initio* calculations were used in combination with this model, and the simulated spectra were found to be in good agreement with the experimental measurements. Two subsequent theoretical studies using the restricted version of the coupled cluster method with single, double, and noniterative triple excitations (RCCSD(T)) have produced more accurate interaction potentials for ArO[20] and ArO^-.[21] Subsequent work simulated the higher resolution ZEKE spectrum of ArO^-,[22] providing motivation for the experimental work described here. Unfortunately, these simulations were affected by a programming error in the intensity calculations. This error, in the symmetry adaptation of the atoms-in-molecule electronic wave functions, led to the absence of many bound−bound transitions in the simulations, a defect that was not apparent by comparison with the broad envelopes of

---

[†] Part of the "George C. Schatz Festschrift".

* To whom correspondence should be addressed. E-mail: (A.A.B.) alexei@classic.chem.msu.su; (D.M.N.) dneumark@berkeley.edu.

[‡] University of California.

[§] Moscow State University.

[||] Oakland University.

[⊥] University of Warsaw.

[#] Lawrence Berkeley National Laboratory.

10.1021/jp8113682 CCC: $40.75

the measured low-resolution PE spectra. The higher resolution experiments presented here have motivated not only a correction of the calculations but also a refined theoretical approach.

In this Article, we present high-resolution photoelectron spectra of ArO^- obtained using SEVI. Numerous well-resolved transitions are observed within the broad envelope of the previous lower resolution photoelectron spectra. Accurate theoretical simulations are presented. The new procedure accounts correctly for all the bound−bound transition intensities and, in addition, includes the contribution of bound−free (dissociative photodetachment) transitions. New potentials for ArO^- and ArO are developed based on an advanced RCCSD(T) level of theory. All these improvements allow us to simulate the SEVI spectrum with high accuracy and help to assign most of its resolved features. Several ArO^- and ArO spectroscopic constants accurately determined from analysis of the experimental spectra are found to be in excellent agreement with the calculated values. Previous PE spectra are also re-examined within the improved theoretical approach to confirm the earlier interpretation and establish the connection with the SEVI measurements.

II. Experimental Section

The SEVI apparatus has been described in detail elsewhere.[7,23,24] SEVI is a variant of anion PE spectroscopy combined with photoelectron imaging[25] in which mass-selected anions are photodetached at a series of wavelengths. The resulting photoelectrons are collected by velocity-map imaging (VMI)[26] using relatively low extraction voltages, with the goal of selectively detecting slow electrons with high efficiency and enlarging their image on the detector. At each wavelength, one obtains a high-resolution photoelectron spectrum over a limited range of electron kinetic energy.

ArO^- anions were produced from of a gas mixture comprising 0.1% N_2O and 10% argon in a balance of neon. The gas mixture, at a stagnation pressure of 350 psi, was expanded into the source vacuum chamber through an Even−Lavie pulsed valve[27] equipped with a circular ionizer. The anions were then perpendicularly extracted into a Wiley−McLaren time-of-flight mass spectrometer[28] and directed to the detachment region by a series of electrostatic lenses and pinholes. A pulse on the last ion deflector allowed only the desired mass into the interaction region. Anions were photodetached between the repeller and the extraction plates of the VMI stack by the gently focused output of a Nd:YAG-pumped tunable dye laser. The photoelectron cloud formed was coaxially extracted down a 50 cm flight tube and mapped onto a detector comprising a chevron-mounted pair of time-gated, imaging quality microchannel plates coupled to a phosphor screen, as is typically used in photofragment imaging experiments.[29] Events on the screen were collected by using a 1024 × 1024 charge-coupled device (CCD) camera and sent to a computer. Electron velocity-mapped images resulting from 30 000 to 50 000 laser pulses were summed, quadrant symmetrized, and inverse-Abel transformed. Photoelectron spectra were obtained via angular integration of the transformed images. The spectra presented here are plotted with respect to electron binding energy (eBE), defined as the difference between the energy of the photodetachment photon and the measured electron kinetic energy (eKE).

The apparatus was calibrated by acquiring SEVI images of atomic oxygen[30] at several different photon energies. In the SEVI experiment, within the same image, all observed transitions have similar widths in pixels (Δr), which means transitions observed further from threshold (larger r) are broader in energy. With the 200 V VMI repeller voltage used in this study, the full widths at half-maximum of the oxygen peaks were 2.2 cm^{-1} at 20 cm^{-1} eKE and 6.8 cm^{-1} at 150 cm^{-1} eKE.

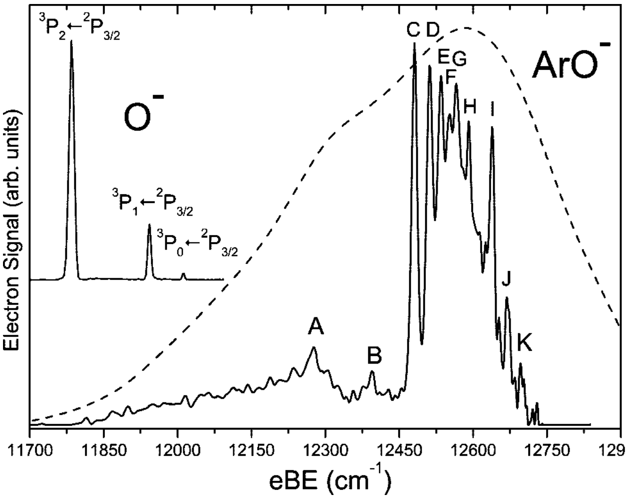

Figure 1. ArO^- SEVI spectrum (solid line) and previous PE spectrum from ref 18 (dashed line) covering the electron binding energy range of 11 700−12 900 cm^{-1}. The SEVI spectrum of O^- is also shown as an inset.

SEVI also provides information on the photoelectron angular distribution (PAD). For one-photon detachment, the PAD is given by[31,32]

$$\frac{d\sigma}{d\Omega} = \frac{\sigma_{\text{total}}}{4\pi}\left(1 + \beta\left(\frac{3}{2}\cos^2\theta - \frac{1}{2}\right)\right) \qquad (1)$$

where θ is the angle between the direction of the photoelectron ejection and the polarization vector of the incident photon. The anisotropy parameter β lies between 2 and −1. It provides information on the orbital angular momentum (l) of the ejected photoelectron and hence the symmetry of the molecular orbital from which detachment occurs; $l = 0$ (s-wave) detachment leads to $\beta = 0$, $l = 1$ (p-wave) to $\beta = 2$, and $l = 0$ and 2 in equal amplitude (s+d-wave) to $\beta = -1$.

III. Experimental Results

The ArO^- SEVI spectrum taken at a photon energy of 12 838.7 cm^{-1} is shown in Figure 1. The spectrum is highly structured, with most transitions occurring between 12 450 and 12 700 cm^{-1}. Clearly discernible peaks are labeled A−K, and their positions are listed in Table 1. The estimated error bars are ±2 cm^{-1}. There are at least two prominent progressions starting with peaks C and I, with characteristic peak spacings of 20−30 cm^{-1}. These progressions appear to lie above a smoothly varying background signal that peaks around 12 550 cm^{-1}, but one cannot tell from the spectrum alone if this background results from spectral congestion or transitions to continuum states of the neutral complex. Signal is also seen below the main features, extending below 12 000 cm^{-1}. A detailed assignment of the SEVI peaks can be made by comparison with the theoretical results presented in section IV.

Figure 1 also shows the previous PE spectrum of de Clercq et al.[18] taken under source conditions generally characterized as “cold”. Comparison of the two spectra illustrates the gain in resolution achieved by SEVI over conventional PE spectroscopy, where only a broad envelope was observed. The region of maximum intensity in the SEVI spectrum approximately

TABLE 1: Experimental and Calculated Peak Positions and Shift from Origin along with Transition Assignments[a]

	experimental		calculated		difference		assignments
peak	eBE	shift	eBE	shift	ΔeBE	Δshift	$n, v \leftarrow n^-, v^-$
A	12 276	−205	12 279.1	−196.6	−3	8	*II*0, 0 ← *II*, 0
B	12 395	−86	12 389.3	−86.4	6	1	*X*2, 0 ← *X*, 1
C	12 481	0	12 475.7	0	5	0	*X*2, 0 ← *X*, 0
D	12 512	31	12 506.3	30.6	6	0	*X*2, 1 ← *X*, 0
E	12 535	54	12 527.0	51.3	8	3	*X*2, 2 ← *X*, 0
F	12 553	72	12 547.5	71.8	6	0	*II*0, 0 ← *X*, 1
G	12 566	85	12 558.8	83.1	7	2	*III*0, 1 ← *X*, 2
H	12 591	110	12 578.1	102.4	13	8	*II*0, 1 ← *X*, 1
I	12 639	158	12 633.9	158.2	5	0	*II*0, 0 ← *X*, 0
J	12 670	189	12 664.6	188.9	5	0	*II*0, 1 ← *X*, 0
K	12 695	214	12 685.3	209.6	10	4	*II*0, 2 ← *X*, 0
a	12 235	−246	12 237.6	−238.1	−3	−8	*X*2, 1 ← *I*, 1
b	12 305	−176	12 310.5	−165.2	−6	−11	*I*0, 0 ← *X*, 2
c	12 330	−151	12 331.6	−144.1	−2	−7	*I*1, 0 ← *X*, 2
d	12 410	−71	12 410.3	−65.4	0	−6	*I*1, 0 ← *X*, 1
e	12 430	−51	12 432.6	−43.1	−3	−8	*I*1, 1 ← *X*, 1

[a] All energies in cm^{-1}. Estimated error bars for peaks A−K are ±2 cm^{-1}.

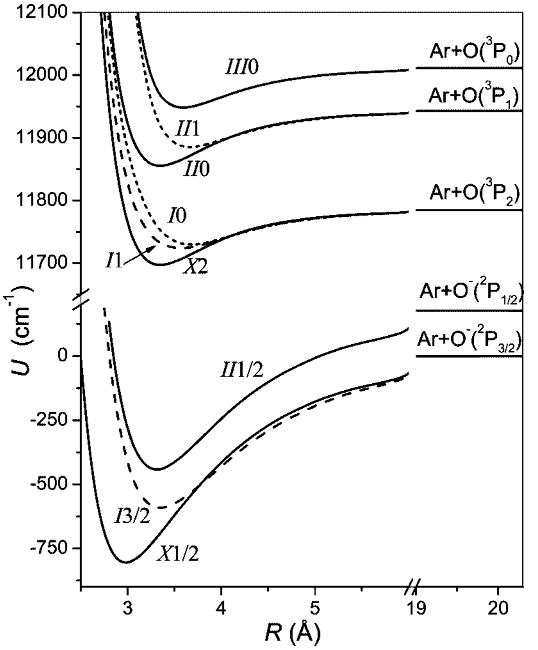

Figure 2. Spin−orbit-coupled potentials of the ArO anion and neutral calculated using the atoms-in-molecule models from the *ab initio* RCCSD(T) AV6Z/bf33221 nonrelativistic potentials.

coincides with the peak of the envelope in the PE spectrum around 12 600 cm^{-1}. However, compared to the PE spectrum, the SEVI spectrum displays much less intensity at eBE < 12 450 cm^{-1}. De Clercq et al.[18] found that intensity in this region was sensitive to ion source conditions and presumably resulted from "hot band" transitions originating from electronically excited anions. Hence, the intensity differences between the SEVI and PE spectra suggest lower anion temperatures in the SEVI experiment.

The SEVI spectrum of O$^-$ taken at 12 092 cm^{-1} photon energy and acquired under similar source conditions as the ArO$^-$ spectrum is also shown in Figure 1. It comprises three well-resolved transitions from the ^{2}P$_{3/2}$ ground spin−orbit state of O$^-$ to the ^{3}P$_{2,1,0}$ spin−orbit states of the neutral, seen at somewhat higher resolution than in recent photoelectron imaging studies.[33] We observed no transitions from the excited ^{2}P$_{1/2}$ excited spin−orbit state of O$^-$, which lies 177.13 cm^{-1} above the ^{2}P$_{3/2}$ state,[30] providing additional confirmation of a low anion temperature in our setup. All the features in the O$^-$ and ArO$^-$ spectra in Figure 1 have β values of 0.0 ± 0.2, indicating an almost pure *s*-wave detachment behavior.

IV. Theory

A. Electronic Structure and Adiabatic Potentials. In order to assign the features in the SEVI spectrum, we have performed *ab initio* calculations on the ArO$^-$ anion and ArO neutral and simulated the spectrum. The electronic structure of these species has been described in detail.[19] In brief, under the nonrelativistic approximation (or *LS* coupling scheme), the interaction of Ar(^{1}S) with O(^{3}P) gives rise to two terms of $^3\Sigma^-$ and $^3\Pi$ symmetry, while the interaction with the O$^-$(^{2}P) anion gives two states of $^2\Sigma^+$ and $^2\Pi$ symmetry. The $^3\Pi$ and $^2\Sigma^+$ states are the lower energy states for the anion and neutral, respectively. We denote the corresponding potentials as V_Σ^-, V_Π^-, V_Σ, and V_Π.[19] Spin−orbit (SO) interaction further splits the molecular terms. For the neutral, there are six SO-coupled states designated as $n\Omega(j)$: *X*2(2), *I*1(2), *I*0(2), *II*1(1), *II*0(1), and *III*0(0), where n indexes the states with the same projection of the total electronic angular momentum j on the molecular axis Ω. Note that j is the asymptotically good quantum number with allowed values 0, 1, and 2. The SO-coupled states of the anion classified using similar $n^-\Omega^-(j^-)$ notation are *X*1/2(3/2), *I*3/2(3/2), and *II*1/2(1/2). For clarity, these electronic states will be denoted only as $n\Omega$ (*X*2, *I*1, *I*0, *II*1, *II*0, and *III*0) for the neutral and as n^- (*X*, *I*, and *II*) for the anion. The asymptotic energies of the terms correlating to Ar + O(^{3}P$_j$) limits referenced to the lowest $j = 2$ term are Δ_j, $\Delta_1 = 158.27$, and $\Delta_0 = 226.98$ cm^{-1}.[34] The Ar + O$^-$(^{3}P$_{1/2}$) limit lies $\Delta^- = 177.13$ cm^{-1} above the ground Ar + O$^-$(^{3}P$_{3/2}$) limit.[30] The lowest anion $j^- = 3/2$ and neutral $j = 2$ limits are separated in energy by the electron affinity (EA) of oxygen atom,[30] EA = 11 784.7 cm^{-1}.

Previously,[19] the V_Σ^-, V_Π^-, V_Σ, and V_Π potentials were calculated using the UMP4 method with the augmented correlation consistent aug-cc-pVnZ (AVnZ), n = T basis set[35] and the 3s3p2d set of bond functions (bf332) placed at the midpoint of internuclear distance *R*. Since then, two refined calculations have been performed. Interaction potentials for RgO (Rg = He−Kr) were computed using the RCCSD(T) method and larger basis set, AVQZ, plus the bf332 augmentation.[20] The calculations of the RgO$^-$ anions for Rg = He−Ar implemented the RCCSD(T) method with the AV5Z basis set.[21] To attain consistent and even better description of the nonrelativistic interactions for ArO and ArO^- species, we used here the RCCSD(T) method and V*n*Z and AV*n*Z bases with $n = 5$ and 6, sometimes augmented by the 3s3p2d2f1g bond function set (bf33221).[36] We also examined the effect of the second-order Douglas−Kroll (DK) relativistic correction (it was applied in combination with the specially optimized AV5Z-DK basis set) and core correlation correlating explicitly the $2p^6$ shell of Ar [normally, as in the previous calculations, the orbitals of $O(1s^2)$ and $Ar(1s^22s^22p^6)$ shells were treated as the core orbitals]. All the potentials mentioned here were corrected for basis set superposition error using the full counterpoise correction.[37]

Equilibrium distances and interaction energies for various *ab initio* potentials mentioned above are presented in Table 2. The new calculations are a significant improvement over the previous UMP4 potentials[19] and agree well with more recent results.[20,21] Saturation of the basis set by the diffuse atomic functions is the most important factor: the V5Z basis unexpectedly gives too deep anion potentials with respect to AV5Z. Further expansion to the AV6Z set and addition of the bond functions provides only minor effects. Neither the scalar relativistic correction under the DK approximation nor the correlation of the Ar $2p^6$ shell are significant. Overall, the results indicate the good convergence of all potentials at the RCCSD(T) AV6Z/bf33221 level of theory, so in what follows we will work with these potentials. For the neutral, they can also be compared to the potentials derived from the beam scattering experiments.[15]

Vectorial SO interaction was introduced using the atoms-in-molecule model that fixes the SO coupling constants at their asymptotic (atomic) values. Explicit expressions for the SO-coupled potentials were given by eqs 7 and 10 in ref 19 (see also refs 15, 16 and 38). The potentials are depicted in Figure 2 and characterized in Table 3. Adiabatic transition energies T_0, dissociation energies D_0, and vibrational constants shown therein were obtained by solving the radial Schrödinger equations numerically for zero rotational angular momentum and fitting the lowest vibrational levels to the Dunham expansion. For the deeper anion potentials, the 10 lowest levels were used, while for the neutral all bound levels supported by the potential (4 or 5) were included.

B. Spectral Simulations. The positions of spectral features, or electron binding energies eBE, are determined by conservation law:

$$E_i + E_0 = E_f + \text{eKE} = E_i + \text{eKE} + \text{eBE} \tag{2}$$

where E_i and E_f are the initial energy of the anion and final energy of the neutral, respectively, and E_0 is the (fixed) photon energy. The transition energy is therefore

$$E = \text{eBE} = E_f - E_i \tag{3}$$

For simplicity and clarity of interpretation, we disregarded rotational structure and considered vibronic bound−bound $n\Omega$, $v \leftarrow n^-$, v^- and bound−free $n\Omega$, $\varepsilon \leftarrow n^-$, v^- transitions, where v^- and v denote the vibrational levels in the particular electronic states of the anion n^- and neutral n, respectively, and ε specifies the kinetic energy of the Ar + $O(^3P_j)$ products above the corresponding dissociation threshold.

The theory underlying the spectral envelope simulations is similar to that presented by Buchachenko et al.,[19] which, in turn, was based on the approach to ZEKE spectral intensities by Zhao et al.[3] The starting point for the bound−bound spectral simulation is eqs 13−16 in ref 19. For the present case, one has

$$I_{if}^{\text{bb}} = I^{\text{bb}}(n\Omega, v \leftarrow n^-, v^-) = \sum_k I_k^{\text{bb}}(n\Omega, v, j_e = 1/2 \leftarrow n^-, v^-) \tag{4}$$

where only *s*-wave electron detachment is considered by setting the total angular momentum of the photoelectron j_e to 1/2. The summation index k corresponds to the combined angular momentum of the photon and photoelectron and runs over 1/2 and 3/2.[3] The vibronic line strength factor is

$$\begin{aligned} I_k^{\text{bb}} &= \left| \langle v | \mu_k(n \leftarrow \Omega n^-) | v^- \rangle \right|^2 \\ &= (2k+1) \left| \sum_{m,\omega} (-1)^{-\mu-\omega-q} \begin{pmatrix} 1/2 & 1 & k \\ \omega & -\mu & q \end{pmatrix} \langle v | T_{n^-n}(1,\mu) | v \rangle \right|^2 \end{aligned} \tag{5}$$

Here, ω and q are the projections of j_e and k angular momenta to the internuclear axis, respectively, and μ denotes the component of the spherical transition dipole moment operator. The electronic transition dipole matrix element $T_{n^-n}(1,\mu)$ is exactly the same quantity that enters similar eq 16 in ref 19

TABLE 2: ***Ab Initio*** **Data on Equilibrium Distances (R_e) and Interaction Energies (D_e) of the Nonrelativistic Potentials of the ArO Anion and Neutral**

	ArO^- ($^2\Sigma^+$)		ArO^- ($^2\Pi$)		ArO ($^3\Pi$)		ArO ($^3\Sigma^-$)	
method[a]	R_e (Å)	D_e (cm^{-1})	R_e (Å)	D_e (cm^{-1})	R_e (Å)	D_e (cm^{-1})	R_e (Å)	D_e (cm^{-1})
V5Z/bf33221	2.945	900	3.346	606	3.355	85.8	3.791	47.1
V5Z-DK/bf33221	2.942	904	3.338	611	3.351	86.1	3.791	47.1
V5Z-DK/bf33221[b]	2.938	907	3.335	614	3.345	86.8	3.786	47.5
AV5Z/bf33221	2.974	851	3.356	591	3.349	87.6	3.785	49.1
AV6Z/bf33221	2.973	852	3.351	592	3.347	87.8	3.781	49.2
AV6Z	2.974	845	3.356	586	3.360	84.8	3.830	47.1
UMP4/AVTZ/bf332[c]	3.013	788	3.408	533	3.384	83.7	3.801	48.2
AVQZ/bf332[d]					3.357	85.8	3.799	48.4
AV5Z[e]	2.975	836	3.358	579				
expt[f]					3.45 ± 0.07	84 ± 8	3.85 ± 0.08	41 ± 4

[a] RCCSD(T) unless otherwise stated. [b] With explicit correlation of the Ar($2p^6$) shell. [c] From ref 19. [d] From ref 20. [e] From ref 21. [f] From ref 15.

and is expressed by eqs 17 and 18 therein. The error mentioned in the Introduction was associated to the parity adaptation of the neutral electronic wave functions in the numerical implementation of these equations and does not affect the analytical formulas.

The bound−free component I^{bf} was calculated in the same way by replacing the bound vibrational function $|v\rangle$ in eq 5 by the continuum function $|\varepsilon\rangle$. The latter was normalized to the semiclassical asymptotic solution to warrant the normalization fully compatible to that of the bound−free component (see, e.g., ref 39 and references therein).

The full spectral envelope was synthesized as

$$S(E) \propto \sum_{i} g_{\mathrm{i}}(T) \int_{-\infty}^{E_0} [I_{\mathrm{if}}^{\mathrm{bb}}(E') + I_{\mathrm{if}}^{\mathrm{bf}}(E';)]\Theta(E - E' + E_{\mathrm{i}})\, \mathrm{d}E' \tag{6}$$

where $g_{\mathrm{i}}(T)$ is the initial state population taken as the equilibrium Boltzmann factor at the single internal temperature T and Θ is the line shape function taken as Gaussian, of the width (fwhm) Γ, multiplied by the factor $(E_0 - E)^{1/2}$ that accounts for the threshold law for s-wave electron detachment.[40]

Setting $I_{\mathrm{if}}^{\mathrm{bb}}(E) = I_{\mathrm{if}}^{\mathrm{bb}}\delta(E_{\mathrm{f}} - E_{\mathrm{i}})$, where δ is the Dirac function, and specifying explicitly electronic and vibrational quantum numbers, one has

$$S(E) \propto \sum_{n-} \sum_{v-} g_{n-v-}(T) \sum_{n\Omega} \Big[\sum_{v} I^{\mathrm{bb}}(n\Omega, v \leftarrow n^- v^-)\, \Theta \\ (E - E_{n\Omega v} + E_{n-v-}) + \int_{-\infty}^{E_0} I^{\mathrm{bf}}(n\Omega, E' \leftarrow n^- v^-)\, \Theta \\ (E - E' + E_{n-v-})\, \mathrm{d}E' \Big] \tag{7}$$

The vibrational wave functions and energies were computed numerically for the adiabatic SO-coupled potentials introduced above. To simulate the bound−bound part of the spectra, transitions to all bound vibronic levels of the neutral from the lowest 10 levels of each anion electronic state were taken into account. This set of initial levels ensures the convergence of the anion partition function at the internal temperatures as high as 400 K. In the simulations of the bound−free components, the transitions from the few lowest anion vibronic levels (X, $v^- = 0-4$; I, $v^- = 0, 1$; II, $v^- = 1$) to all adiabatic continua were included. The I^{bf} function was represented on a uniform grid of energies from E_{min} to E_0, where E_{min} corresponds to the energy of the lowest threshold in the set. Integration in eq 7 was performed using the Simpson one-third rule.

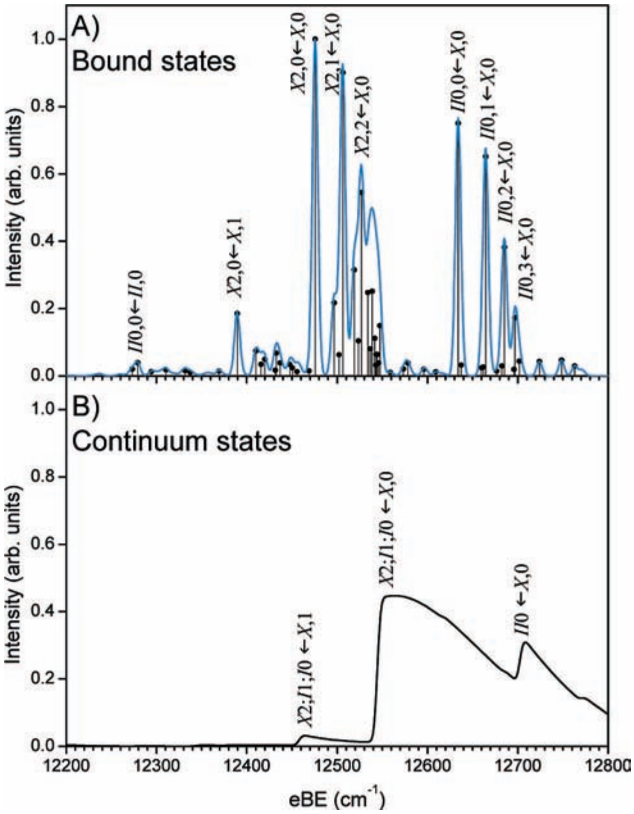

Figure 3. Simulated spectrum at $T = 50$ K and $\Gamma = 5$ cm^{-1} showing transitions to bound states (top panel) and continuum states (bottom panel).

TABLE 3: Parameters of the SO-Coupled Potentials of the ArO Anion and Neutral Calculated Using the *Ab Initio* Nonrelativistic AV6Z/bf33221 Potentials

state	R_{e} (Å)	D_{e} (cm^{-1})	T_0 (cm^{-1})	D_0 (cm^{-1})	ω_{e} (cm^{-1})	$\omega_{\mathrm{e}}x_{\mathrm{e}}$ (cm^{-1})
			ArO$^-$			
X	2.976	805.9	0	759.7	89.3	2.87
I	3.351	592.2	202.6	557.1	67.6	2.30
II	3.318	620.4	354.9	581.9	76.4	2.66
			ArO			
*X*2	3.347	87.8	12 475.7	68.6	38.5	4.34
*I*1	3.559	61.3	12 496.7	47.6	28.5	3.35
*I*0	3.659	55.6	12 502.3	42.0	26.9	3.30
*II*1	3.647	58.2	12 659.9	42.7	30.7	4.23
*II*0	3.347	87.8	12 634.0	68.6	38.5	4.34
*III*0	3.569	63.9	12 724.0	47.3	30.7	3.83

Preliminary adjustment indicated that the values $\Gamma = 5$ cm^{-1} and $T = 50$ K provide good representation for the observed SEVI spectrum. The resulting simulated spectral envelope is shown in Figure 3. The bound−bound and bound−free transitions are presented in panels A and B, respectively, of Figure 3. In Figure 3A, the vertical lines represent the positions and intensities of the individual bound−bound vibronic transitions with the more intense being explicitly identified as $n\Omega$, $v \leftarrow n^-$, v^-. Similarly, in Figure 3B, the bound−free transitions are denoted as $n\Omega \leftarrow n^-$, v^-. It can be seen from Figure 3A that the bound−bound simulated spectrum is dominated by two bands of peaks that are transitions from the anion ground level to the various vibrational levels of the neutral $X2$ and $II0$ states. This result reflects the selectivity of the spin−orbit transitions but also the fact that these two states have an equilibrium geometry more similar to the anion ground-state than the equilibrium geometries of the other neutral states (see Figure 2 and Table 2). The bound vibrational wave functions of the $X2$ and $II0$ states thus have larger Franck−Condon overlap with the anion ground state. The simulated bound−free spectrum is dominated by two main features. The larger feature at 12 565 cm^{-1} is composed of transitions from the anion ground level to the $X2$, $I1$, and $I0$ continuum states. Similarly, the second feature at 12 712 cm^{-1} is composed of transitions from the anion ground level to the $II0$ continuum.

V. Analysis and Discussion

A. Peak Assignments and Comparison with Theory. Figure 4 compares the ArO$^-$ SEVI spectrum and the full simulation, including both panels in Figure 3. Overall, the simulated and experimental spectra agree reasonably well, facilitating the assignment of most of the features. The resulting

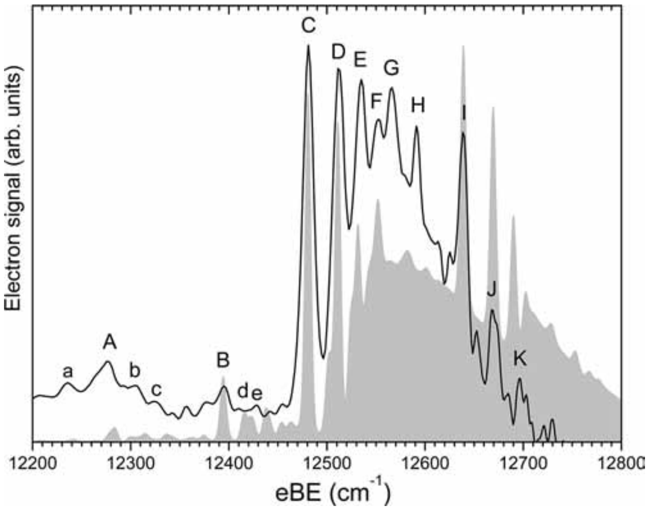

Figure 4. Comparison of the experimental (black line) and simulated (shadowed) ArO$^-$ SEVI spectrum in the 12 200−12 800 cm^{-1} electron binding energy range.

assignments of peaks A−K in the SEVI spectrum are listed in Table 1, along with the experimental and calculated position of each peak. Peak C at 12 481 cm^{-1} is assigned to the $X2$, 0 ← X, 0 origin transition. This value is the electron affinity EA for ArO and is in very good agreement with the calculated value of 12 475.7 cm^{-1}. The shifts of all experimental and calculated peaks relative to this transition are given in Table 1, as is the difference between the experimental and calculated shift for each peak, in the "Δshift" column. These differences are 8 cm^{-1} for the small peaks A and H, and 4 cm^{-1} or less for the remaining peaks.

Peaks D and E are thus assigned to the $X2$, v ← X, 0 transitions with $v = 1$ and 2, respectively. Peaks I, J, and K are assigned to the $II0$, v ← X, 0 progression with $v = 0$, 1, and 2, respectively. The positions of the observed levels on these two states are consistent with the atoms-in-molecule model[19] used here. In this model, the potential energy curves of the neutral $X2$ and $II0$ state are only defined by the $^2\Pi$ potential, with the two curves being separated by the 158.27 cm^{-1} $^3P_1$−$^3P_2$ oxygen spin−orbit splitting (Δ_1). In agreement with the calculations, the splitting between peaks C and I in the SEVI spectrum, which is the separation between the vibrational ground-state levels of the $X2$ and $II0$ states, is found to be 158 cm^{-1}. We also find an identical fundamental vibrational frequency of 31 cm^{-1} for both states which is in excellent agreement with the calculated value, 30.6 cm^{-1}. However, the experimental frequency of the $v = 2$ levels in these two states is found to be 3−4 cm^{-1} above the 51.3 cm^{-1} calculated value. This indicates that the calculations slightly overestimate the anharmonicity of the interaction potential for these two particular states.

All the remaining peaks in the SEVI spectrum are assigned to hot band transitions, with most of them originating from the first excited vibrational level of the anion ground electronic state. Peaks B and F are assigned to the transitions to $X2$, 0 and $II0$, 0 neutral levels from the X, 1 level of the anion, respectively. The splitting between peaks F and I is the same that that between peaks B and C and thus yields an experimental fundamental frequency of 86 cm^{-1} for the X anionic ground-state. This is again in excellent agreement with the 86.4 cm^{-1} calculated value.

Peak A at 12 276 cm^{-1} is assigned to the $II0$, 0 ← II, 0 transition and is the only well resolved feature originating from one of the two low-lying anionic excited states. The separation between peaks A and I thus yields an experimental term energy of 363 cm^{-1} for the II anion state which is slightly larger than the calculated value of 354.9 cm^{-1}. There are several smaller peaks in the vicinity of peaks A and B, labeled a−e in Figure 4, that line up well with smaller features in the simulation from vibrational hot bands. Based on this correspondence, as well as on the results of simulations at higher temperatures in the next subsection, peaks a−e are also assigned in Table 1, but these assignments must be considered as quite tentative owing to the poor signal-to-noise associated with these small features.

Peaks G and H are more difficult to assign. They occur in a spectral region where the simulated bound−bound spectrum is very weak (see Figure 3A) but where detachment to the Ar + O continuum is substantial. Based on calculated peak positions alone (and not intensities), peak G can be tentatively assigned to the $III0$, 1 ← X, 2 transition and peak H to the $II0$, 1 ← X, 1 transition. As shown in Table 1, the deviations between calculated and experimental peak positions are quite small, particularly when the "shifted" calculated energies are used. An alternative assignment, however, should also be mentioned. Peaks G and H are separated by 25 cm^{-1}, which is the same spacing found between peaks D and E (23 cm^{-1}) and J and K (25 cm^{-1}), suggesting that they, like peaks J and K, may represent transitions to the $v = 1$ and 2 levels of the $II0$ neutral state (which, as discussed above, has the same vibrational level spacings as the $X2$ neutral state). Peaks G and H could originate from the $v = 0$ level of the anion $I3/2$ state, but this assignment would imply a term value $T_0 = 104$ cm^{-1} for that state, which is considerably lower than the calculated value of 202.6 cm^{-1} in Table 3. This, in turn, would require that the dissociation energy of the ArO$^-$ $^2\Pi$ state be increased by around 100 cm^{-1} compared to the calculated value of 592 cm^{-1} in Table 2, which seems excessively large. Hence, the assignments in Table 1 are preferred at present.

It can be seen from the previous discussion and from Table 3 that the calculated peak positions and spectroscopic constant are in good overall agreement with the experimental values. This agreement confirms the reliability of the *ab initio* calculations and the spin−orbit treatment used here for the ArO and ArO$^-$ interaction potentials. While the peak positions agree very well, the simulated spectrum displays some noticeable intensity differences from the SEVI spectrum, particularly at high eBE where the continuum contribution appears larger in the simulations than in the experiment. There are many factors that may affect the accuracy of the intensity calculations. Small inaccuracies in the interaction potentials are likely responsible for the overly slow falloff of the continuum at high eBE. Assumption of single-temperature Boltzmann equilibrium as well as the use of single line width parameter for all transitions, including the bound−free ones, are hard to justify *ad hoc*. The theory[19] used for the photodetachment transition dipole matrix elements in eq 5 does not accurately capture threshold behavior that may affect the intensity not only close to E_0 but also close to the onset of bound−free transitions.

B. Simulations of Previous PE Spectra. As was already mentioned, conventional photoelectron (PE) spectra of the complexes formed by the O$^-$ anion with Ar, Kr, Xe, and N_2 were obtained by de Clercq et al.[18] These spectra, recorded at significantly lower resolution (∼200 cm^{-1}), have a bimodal structure. Two broad peaks alter their relative intensity depending on the expansion source conditions that correspond

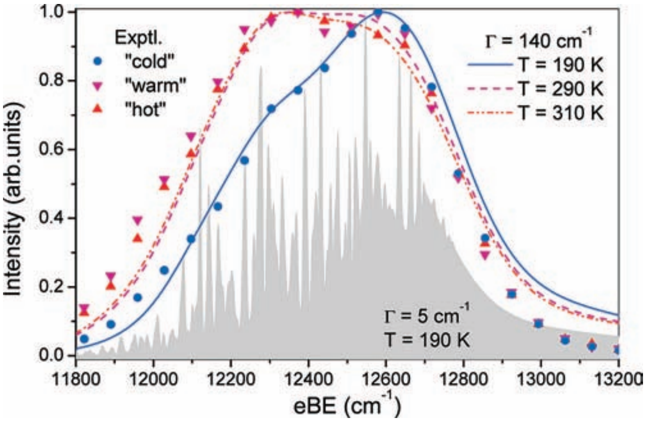

Figure 5. Comparison of the experimental[18] and simulated ArO$^-$ PE spectra at three expansion source conditions or temperatures. Shadowed spectrum is simulated at "cold" conditions (190 K) with the SEVI resolution of 5 cm^{-1}.

to production of "cold", "warm", and "hot" anions (see Figure 5). Theoretical analysis of these spectra[19,41] was limited by inaccuracy in the interaction potentials and the error in transition intensity calculation mentioned above that may have led to misinterpretation. Therefore, we performed refined spectral simulations with the same set of transitions as were used for the SEVI simulations, varying only the anion temperature and the Gaussian line width. The spectra simulated with the experimental line width of 200 cm^{-1} always appear as a single broad peak that moves toward lower electron binding energy as the temperature increases. However, the use of a smaller width, $\Gamma = 140$ cm^{-1}, provides very reasonable agreement with experiment: as temperature grows from 190 to 310 K, the spectral envelope evolves from higher to lower energy, passing through the bimodal pattern as shown in Figure 5. The positions of both peaks agree very well with the experiment. The reduction of line width can be explained by the "broadening" of simulated spectra due to exaggeration of discrete-continuum contribution, as follows from the analysis of the SEVI spectrum.

To illustrate the connection between the PE and SEVI spectra, we also present in Figure 5 the spectrum simulated at "cold" (190 K) temperature and SEVI resolution ($\Gamma = 5$ cm^{-1}). Above eBE = 12 450 cm^{-1}, this simulation reveals the same transitions as does the true SEVI spectrum. Among them, hot-band transitions forming peaks F, G, and H gain intensity with respect to the transitions from the anion ground-state represented by peaks C, D, and E. The $II0, 0 \leftarrow X, 1$ transition (peak F) determines the position of the high-energy feature of the PE spectrum. At lower eBE, between 12 250 and 12 450 cm^{-1}, two of the three most prominent features are also seen in the SEVI spectrum as the weak peaks A, B and d, e. Most of the transitions falling in this region, which determine the low-energy peak in the PE spectra, originate either from the first anion excited state $I3/2$ or from vibrationally excited levels of the anion ground state X. The group of features appearing below peak A (12 280 cm^{-1}) corresponds to the transitions from the second excited state II with admixtures of transitions from highly excited vibrational levels of the X and I states. It should be noted that although previous theoretical interpretation of the ArO$^-$ PE spectra by Buchachenko et al.[19] was wrong in the detailed assignment of individual transitions, the main conclusion[18] that two peaks generally correspond to two states of the anion, X and I, remains valid.

VI. Conclusion

The high-resolution photoelectron spectrum of ArO$^-$ obtained using the slow electron velocity-map imaging technique is reported. New high level *ab initio* calculations on the ArO$^-$ and ArO are presented and used in combination with an atom-in-molecule model to simulate the SEVI spectrum. Several ArO$^-$ and ArO vibrational frequencies and excited-state term energies are accurately determined from the analysis of the experimental spectra and are found to be in excellent agreement with the calculated values. The theoretical analysis of the previous PE spectrum of ArO$^-$ has also been revised in the light of the new *ab initio* calculations and spectral simulations.

Acknowledgment. We thank Dr. Andrey Stolyarov for useful comments concerning the normalization of the bound−free spectra. This work was supported by the Air Force Office of Scientific Research under Grant No. F49620-03-1-0085 (D.M.N.), the National Science Foundation under Grant No. CHE-0719260 (M.M.S. and G.C.), and the Russian Basic Research Fund under Project No. 08-03-00414 (A.A.B.). E.G. thanks the National Science and Engineering Research Council of Canada (NSERC) for a post graduate scholarship, and T.I.Y. thanks the Fonds Québécois de la Recherche sur la Nature et les Technologies (FQRNT) for a master's scholarship.

References and Notes

(1) Rienstra-Kiracofe, J. C.; Tschumper, G. S.; Schaefer, H. F.; Nandi, S.; Ellison, G. B. *Chem. Rev.* **2002**, *102*, 231.

(2) Kitsopoulos, T. N.; Waller, I. M.; Loeser, J. G.; Neumark, D. M. *Chem. Phys. Lett.* **1989**, *159*, 300.

(3) Zhao, Y. X.; Yourshaw, I.; Reiser, G.; Arnold, C. C.; Neumark, D. M. *J. Chem. Phys.* **1994**, *101*, 6538.

(4) Yourshaw, I.; Lenzer, T.; Reiser, G.; Neumark, D. M. *J. Chem. Phys.* **1998**, *109*, 5247.

(5) Lenzer, T.; Yourshaw, I.; Furlanetto, M. R.; Reiser, G.; Neumark, D. M. *J. Chem. Phys.* **1999**, *110*, 9578.

(6) Aquilanti, V.; Cappelletti, D.; Lorent, V.; Luzzatti, E.; Pirani, F. *J. Phys. Chem.* **1993**, *97*, 2063.

(7) Neumark, D. M. *J. Phys. Chem. A* **2008**, *112*, 13287.

(8) Powell, H. T.; Murray, J. R.; Rhodes, C. K. *Appl. Phys. Lett.* **1974**, *25*, 730.

(9) Dunning, T. H.; Hay, P. J. *J. Chem. Phys.* **1977**, *66*, 3767.

(10) Langhoff, S. R. *J. Chem. Phys.* **1980**, *73*, 2379.

(11) Aquilanti, V.; Liuti, G.; Pirani, F.; Vecchiocattivi, F.; Volpi, G. G. *J. Chem. Phys.* **1976**, *65*, 4751.

(12) Aquilanti, V.; Casavecchia, P.; Grossi, G.; Lagana, A. *J. Chem. Phys.* **1980**, *73*, 1173.

(13) Aquilanti, V.; Grossi, G. *J. Chem. Phys.* **1980**, *73*, 1165.

(14) Aquilanti, V.; Luzzatti, E.; Pirani, F.; Volpi, G. G. *J. Chem. Phys.* **1980**, *73*, 1181.

(15) Aquilanti, V.; Candori, R.; Pirani, F. *J. Chem. Phys.* **1988**, *89*, 6157.

(16) Ma, Z.; Liu, K.; Harding, L. B.; Komotos, M.; Schatz, G. C. *J. Chem. Phys.* **1994**, *100*, 8026.

(17) Arnold, S. T.; Hendricks, J. H.; Bowen, K. H. *J. Chem. Phys.* **1995**, *102*, 39.

(18) de Clercq, H. L.; Hendricks, J. H.; Bowen, K. H. *J. Chem. Phys.* **2002**, *117*, 2619.

(19) Buchachenko, A. A.; Jakowski, J.; Chalasinski, G.; Szczesniak, M. M.; Cybulski, S. M. *J. Chem. Phys.* **2000**, *112*, 5852.

(20) Krems, R. V.; Buchachenko, A. A.; Szczesniak, M. M.; Klos, J.; Chalasinski, G. *J. Chem. Phys.* **2002**, *116*, 1457.

(21) Viehland, L. A.; Webb, R.; Lee, E. P. F.; Wright, T. G. *J. Chem. Phys.* **2005**, 122.

(22) Buchachenko, A. A.; Szczesniak, M. M.; Chalasinski, G. *Chem. Phys. Lett.* **2001**, *347*, 415.

(23) Osterwalder, A.; Nee, M. J.; Zhou, J.; Neumark, D. M. *J. Chem. Phys.* **2004**, *121*, 6317.

(24) Zhou, J.; Garand, E.; Neumark, D. M. *J. Chem. Phys.* **2007**, *127*, 114313.

(25) Sanov, A.; Mabbs, R. *Int. Rev. Phys. Chem.* **2008**, *27*, 53.

(26) Eppink, A.; Parker, D. H. *Rev. Sci. Instrum.* **1997**, *68*, 3477.

(27) Even, U.; Jortner, J.; Noy, D.; Lavie, N.; Cossart-Magos, C. *J. Chem. Phys.* **2000**, *112*, 8068.

(28) Wiley, W. C.; McLaren, I. H. *Rev. Sci. Instrum.* **1955**, *26*, 1150.

(29) Chandler, D. W.; Houston, P. L. *J. Chem. Phys.* **1987**, *87*, 1445.

(30) Neumark, D. M.; Lykke, K. R.; Andersen, T.; Lineberger, W. C. *Phys. Rev. A* **1985**, *32*, 1890.

(31) Cooper, J.; Zare, R. N. *J. Chem. Phys.* **1968**, *48*, 942.

(32) Reid, K. L. *Annu. Rev. Phys. Chem.* **2003**, *54*, 397.

(33) Cavanagh, S. J.; Gibson, S. T.; Gale, M. N.; Dedman, C. J.; Roberts, E. H.; Lewis, B. R. *Phys. Rev. A* **2007**, 76.

(34) Ralchenko, Y.; Kramida, A. E.; Reader, J. *NIST Atomic Spectra Database*, version 3.1.5; National Institute of Standards and Technology: Gaithersburg, MD, 2008.

(35) Woon, D. E.; Dunning, T. H. *J. Chem. Phys.* **1993**, *98*, 1358.

(36) Cybulski, S. M.; Toczylowski, R. R. *J. Chem. Phys.* **1999**, *111*, 10520.

(37) Boys, S. F.; Bernardi, F. *Mol. Phys.* **1970**, *19*, 553.

(38) Krems, R. V.; Buchachenko, A. A. *J. Phys. B: At., Mol. Opt. Phys.* **2000**, *33*, 4551.

(39) Herman, P. S.; Sando, K. M. *J. Chem. Phys.* **1978**, *68*, 1153.

(40) Wigner, E. P. *Phys. Rev.* **1948**, *73*, 1002.

(41) Buchachenko, A. A.; Szczesniak, M. M.; Klos, J.; Chalasinski, G. *J. Chem. Phys.* **2002**, *117*, 2629.

JP8113682